Citation
Javed, U. and Shaikh, F.U.A. and Sarker, P.K. 2022. Microstructural investigation of thermo-mechanically processed lithium slag for geopolymer precursor using various characterization techniques. Construction and Building Materials. 342: ARTN 127952. http://doi.org/10.1016/j.conbuildmat.2022.127952

Microstructural investigation of thermo-mechanically processed lithium slag for geopolymer precursor using various characterization techniques

Usman Javed, Faiz Uddin Ahmed Shaikh* and Prabir Kumar Sarker
School of Civil and Mechanical Engineering, Curtin University, Perth, Australia.
*Corresponding author: s.ahmed@curtin.edu.au

Abstract

Lithium slag is an emerging industrial waste due to the increasing demand for lithium rechargeable batteries attributed to the recent boom in the automobile industry and space exploration. It is extracted as a powder residue in sedimentary tanks after the refining process of lithium extraction. In this study, the effect of thermo-mechanical processing on the chemical reactivity of lithium slag is assessed by TESCAN Integrated Mineral Analyzer (TIMA), X-ray Fluorescence (XRF), Rietveld quantitative refinement techniques. The chemical, mineral, and crystallographic phase composition of processed lithium slag specimens were assessed and compared by XRF, TIMA, and Rietveld quantitative refinement techniques, respectively. The results of thermo-mechanical processing indicated that the mineral and crystallographic transformation of Spodumene to feldspars (Anorthite, Muscovite, Albite) occurred by crystallite agglomeration. The chemical reactivity of lithium slag is gauged in terms of amorphous alumino-silicates present in feldspars and unidentified phases. Characterization of unidentified phase is evident that it majorly contains micro-nano sized alumino-silicate rich particles with similar spectral signatures to that of feldspar, some fraction of it is aggregated into other phases due to its reactivity. The concentration of the amorphous phase is proportionate with the thermo-mechanical processing energy. However, the thermo-mechanical processing energy is also optimized based on the generation of amorphous phase and reduction in particle size. Therefore, the G1C700 processed regime resulted in one of the maximum amounts of amorphous phase (52.60%). The mineral phase transformation of Spodumene to Anorthite (+10.46%) and unidentified phase (+8.24%) along with D_{50} value of 13.26 μm, consequently releasing 0.45 kg of carbon emissions upon thermo-mechanical

processing. Hence, G1C700 lithium slag is recommended for its use as a geopolymer precursor.

Abbreviations:

TIMA, TESCAN Integrated Mineral Analyzer; XRF, X-ray Fluorescence; USGC, United States Geological Survey; Ca/(Si+Al), Calcium to Cumulative Silica and Alumina Ratio; XRD, X-ray Diffraction; ASTM, American Society for Testing Materials; SEM, Scanning Electron Microscopy; EDS, Energy Dispersive X-ray Spectroscopy; BSE, Back-Scattered Electron

Keywords: Lithium slag; Thermo-mechanical processing; Amorphous alumino-silicates; Tescan Integrated Mineral Analysis; Rietveld quantitative refinement; Geopolymer precursor

1. Introduction

Lithium is one of the prime minerals which has its applications in various fields as a sustainable power storage source such as lithium-ion batteries due to its high energy density and electrochemical potential [1]. Lithium has found its applications in electric vehicles in the automobile industry and emerging space technology. Besides batteries, it has also been used in ceramics, metallurgy, chemicals, and pharmaceuticals [2]. Lithium occurs in the form of brines, volcanic deposits (hectorite clay minerals), and pegmatites. Australia holds 18% of the world's lithium resources after Chile (48%) and China (20%) [3]. Lithium resources in Australia are found in the form of Spodumene ore at Greenbushes, Mount Marion, Earl Grey, Pilgangoora, and Wodgina with the approximate lithium resource of 1320, 180, 525, 790, and 240 kilotons, respectively [3]. The global lithium concentrate production from mining sources was 1.803 million metric tonnes in 2017 as reported by the United States Geological Survey (USGS) [4]. The lithium ore refining process produces approximately 673 kt of lithium slag each year in Australia which is usually disposed of on open-air dumping sites. This may cause air-borne health-hazardous particulate matter in the atmosphere [5]. The abrupt increase in demand for lithium in recent years has projected a higher amount of lithium slag generation along with its safe disposal risks.

Despite raw lithium slag having a higher cumulative concentration of alumina and silica, the crystalline nature of alumino-silicate minerals reduces its degree of reactivity [6]. Moreover, the acid roasting of Spodumene ore during the lithium refining process produces over 6% of sulfate content (SO_4^{-2}) [7], which limits its usage as a pozzolan in cement concrete production [8-10]. Therefore, lithium slag might be used as a precursor in a geopolymer binder system. The reactivity of lithium slag is dominated by the presence of alumino-silicates in desired chemical proportions and the presence of an amorphous phase. The hydration reactivity and pozzolanic potential of a binder depending on the Ca/(Si+Al) ratio. Supplementary cementitious material is termed as hydration reactive if the ratio is 1, else it is termed as pozzolanic reactive if this ratio is lower than 1 [11]. As per the published statistical studies on the

chemical composition of lithium slag, its chemical composition resembles that of fly ash along with Ca/(Si+Al) ratio ranging between 0.002 and 0.368 which is much lower than those of cement (2.022-2.994) and blast furnace slag (0.559-2.321)[7]. The presence of the amorphous phase in raw lithium slag induces some degree of reactivity in it since it was formed by thermo-mechanical processing of Spodumene for lithium extraction [7]. The amorphous phase in lithium slag is composed of fragmented particles of alumino-silicates originating from various minerals fused by the process of agglomeration [7, 12]. The concentration of the amorphous phase can be enhanced in lithium slag by the combined effect of calcination and grinding.

It is a fact that the reactivity of a mineral depends mainly on its particle size, chemical composition, and crystallographic characteristics. Thermal, mechanical, and combination of both thermal and mechanical processing regimes have the potential to change the crystallographic orientation, crystallite size, mineralogical composition, and most importantly the reactivity of aluminosilicates in powders [12]. Thermal treatment specifically at temperatures lower than the melting point of Spodumene transform the crystal structure and orientation upon sintering [13]. Only a few studies recently investigated the performance of lithium slag as a precursor in geopolymer binder, however, the detailed microstructural morphology, mineral, and crystallographic phase transformation of thermo-mechanically processed lithium slag has not been investigated before. Moreover, the quantification and characterization of amorphous phase in processed lithium slag is determined to assess its reactivity.

Therefore, the current research investigates the separate and combined effect of grinding and calcination on the reactivity of lithium slag-based geopolymer precursors. The effect of thermo-mechanical processing on reactivity and mineral phase transformation of lithium slag is studied by quantification of its mineralogical and crystallographic phases by TIMA and X-ray diffraction (XRD), respectively. The mineral composition of processed lithium slag is verified and endorsed by the results of XRF (quantitative). The particles size distribution was compared with both laser diffraction technique and Energy Dispersive X-ray Spectroscopy (EDS) in which

particles sizes were determined by identifying particle boundaries from backscattered spectra. Moreover, the effect of crystallographic, mineral phase transformation, and formation of amorphous phase upon thermo-mechanical processing is also studied.

2. Materials and Methods

The lithium slag used in this study was supplied from a local lithium refinery plant-based in Western Australia which was discharged in sedimentation tank after sulfation process. The oxide composition of raw lithium slag is shown in Table 1. The loss on ignition value of 6.76% may be considered relatively high which indicates the dihydroxylation of phyllosilicate minerals [14]. The cumulative sum of alumina, silica, and iron oxide is 77.06% qualifying as a mineral admixture as per ASTM C618 [15].

2.1.Mechanical and thermal treatment

Lithium slag was subjected to mechanical grinding and calcination. Due to the hygroscopic nature of lithium slag, it was oven-dried at 105˚C before processing. The grinding of lithium slag was conducted for 1 and 2 hrs in a ball mill with the lithium slag to charge ratio of 1:10. For optimizing grinding energy, 70 and 30% weight of stainless-steel balls of 50 and 25-mm diameter, respectively along with a rotation speed of 55 rpm was selected in grinding operation. The lithium slag was calcined for devitrification (phase conversion below the melting point) of distinct alumino-silicate minerals into amorphous phases [16]. Liu et al. [17] reported the maximum formation of the amorphous phase in lithium slag at 700˚C. The calcination temperature was brought up to 700˚C at the rate of 3˚C/min and held there for two hours in a muffle furnace, which was subsequently cooled by natural convection instead of quenching to allow the higher degree of phase separation as shown in Figure 1 [18]. The effect of calcination on the reactivity of lithium slag before grinding and after grinding is assessed, thus the various processing arrangements of lithium slag are presented in Table 2.

Table 1: Chemical oxide quantification of raw lithium slag by X-ray Fluorescence

Oxides	SiO_2	Al_2O_3	Fe_2O_3	CaO	MgO	MnO	TiO_2	SO_3	P_2O_5	K_2O	Na_2O	LOI
Raw Lithium slag	54.53	21.08	1.45	7.535	0.575	0.23	0.05	5.62	0.238	0.884	0.72	6.76

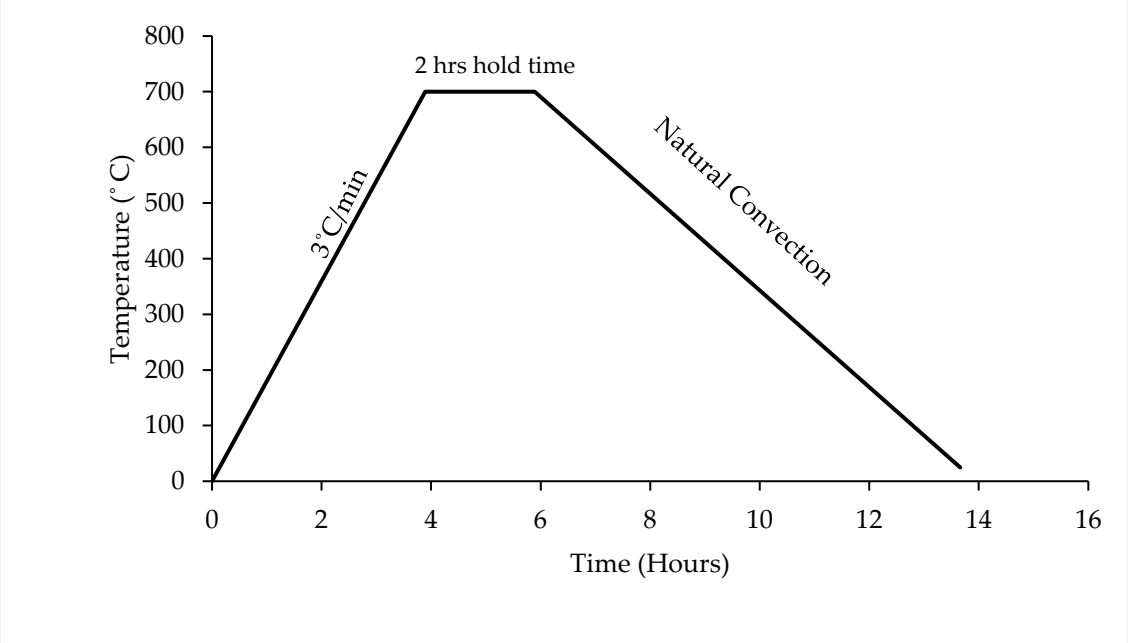

Figure 1: Calcination regime for thermal treatment of lithium slag

Table 2: Mechanical and thermal processing schematics of lithium slag

Abbreviations	**Processing Scheme**
Raw-LS	Raw lithium slag
G1	Lithium slag ground for 1 hour
G2	Lithium slag ground for 2 hours
G1C700	Lithium slag ground for 1 hour, followed by calcination at 700˚C
G2C700	Lithium slag ground for 2 hours, followed by calcination at 700˚C
C700G1	Calcination of raw lithium slag at 700˚C followed by grinding for 1 hour
C700G2	Calcination of raw lithium slag at 700˚C followed by grinding for 2 hours

2.2.Automated-Scanning Electron Microscopy (SEM)

Automated Scanning Electron Microscopy (SEM) aided with EDS was conducted on resin-impregnated polished processed lithium slag specimens by a Tescan Integrated Mineral Identification Analyzer. TIMA is equipped with high-resolution Field Emission Scanning Electron Microscopy, four fully integrated EDS detectors,

secondary electron and Back-Scattered Electron (BSE) detectors that have the ability of data collection in a fully automated mode. Secondary electrons collect and form the image containing topographic details, whereas backscattered electrons being elastically scattered possess energy closer to that of the primary electron beam's energy which images the compositional data of identified phases [19]. Moreover, heavier elements and compounds appeared brighter on the backscattered micrograph than that of the lighter one. However, the combination of BSE greyscale difference and EDS data is used to identify the mineralogical phases' boundaries and quantify the mineral compositions, respectively [19, 20]. Moreover, the identification of particle boundaries and phase compositions is based on mineralogical spectral signatures [21].

TIMA has the potential ability to quantify the percentage minerals, distribution of elemental composition in minerals, mineral association, and mineral grain size distribution [19]. It is a fact that the grinding and calcination results in the formation of amorphous/unidentified phases by the cumulative effect of aggregation and agglomeration [22]. However, the mineral liberation analysis was conducted on epoxy impregnated resin blocks containing processed lithium slag for identification and quantification of the mineral phases, grain size distribution, and analyzing the effect of thermo-mechanical processing on the reactivity of lithium slag by classifying unidentified phases.

2.2.1. Sample preparation

The thermo-mechanically processed lithium slag powder specimens were epoxy impregnated with EpoFix resin on a CitoVac mounting machine (Struers) for perfect removal of air pockets in voids, cracks, and fissures, the presence of which can potentially affect the mineral quantification [23]. For accurate quantification of mineralogy, epoxy impregnated processed lithium slag specimens were ground and polished on Stuers Tegramin-30. The grinding operation was performed to level the surface up to a mean grain size of 9 micrometers followed by polishing for a maximum of 1-micrometer undulation. Resin blocks were carbon-coated (20 nm) in a Cressington 208C carbon coater.

2.2.2. Test parameters

The testing parameters for automated SEM-EDS conducted in TIMA were kept constant for all lithium slag specimens which are shown in Table 3. Mineral liberation analysis was performed for identification, distribution, and quantification of mineral phases throughout the polished resin surface. Electron beam energy, probe current, and beam intensity was kept at 25 KeV, 5.43 nA, and 18.99 nm, respectively. Whereas the high-resolution mode of dot scanning was selected along with the spot size, working distance, and pixel size of 85.18 nm, 15 mm, and 1μm, respectively. The analysis time for mineral identification is related to the X-rays acquisition time at one-micron pixel size, thus the scanned polished area of particles. Therefore, the analysis time is linearly related to the X-rays acquisition time of each pixel of 1-micron size with the regression coefficient (R) of 0.93 as shown in Figure 2.

Table 3: Mineral identification of over three million particles of processed lithium slag on Field Emission TESCAN Integrated Mineral Identification

Sr. No	TIMA Parameters	Raw-LS	G1	G2	G1C700	G2C700	C700G1	C700G2
1	Analysis Time (hrs)	4.69	4.67	6.45	7.65	5.84	6.05	5.52
2	X-ray acquisition points (millions)	5.86	5.17	6.84	8.28	6.52	6.81	5.97
3	Analysis Type	Mineral Liberation Analysis						
4	Beam energy	25 KeV						
5	Probe current	5.43 nA						
6	Beam intensity	18.99 nm						
7	Spot size	85.18 mm						
8	Working distance	15 mm						
9	Resolution (Pixel Size)	1 μm						
10	Acquisition Mode	Dot Mapping						

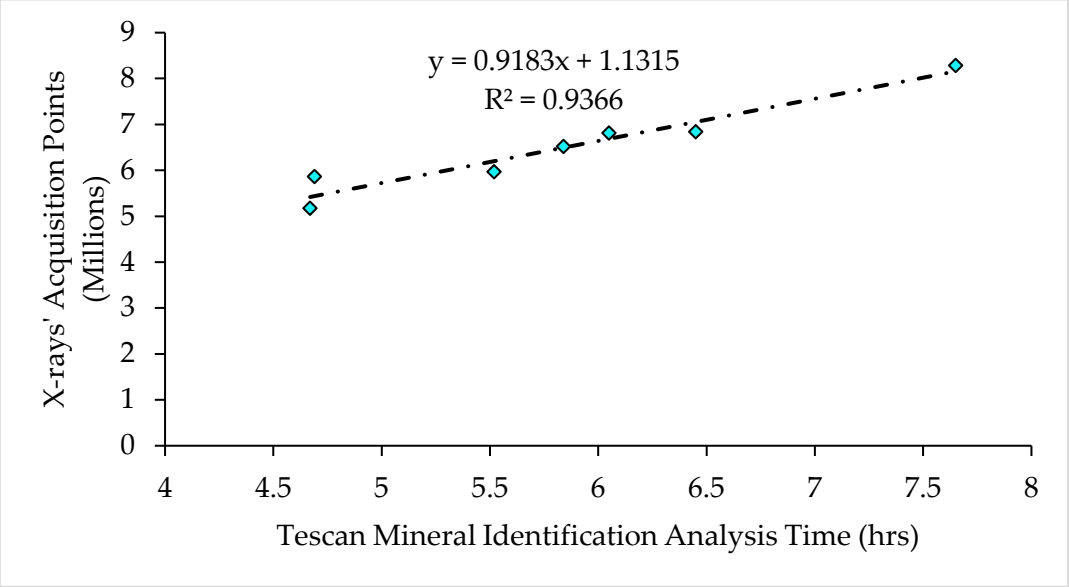

Figure 2: Relation between automated SEM scan time and X-rays' acquisition points

2.3.X-ray diffraction and Rietveld quantitative analysis

X-ray diffraction of processed lithium slag was performed on robotic arm-based Bruker D8 Advance diffractometer with Cu_Kα (1.504Å) radiation source operated at 40 mA and 35 kV. Peak crystallographic phases were identified using DIFFRAC EVA software using International Crystallographic Diffraction Data (ICDD, PDF-2 release 2019). Crystal phase quantification of thermo-mechanically processed lithium slag specimens was performed by adding 50% of Corundum (Al_2O_3) by weight as internal standard and Rietveld analysis was performed using TOPAS (Bruker AXS) version 5 software. All selected parameters for conducting XRD and Rietveld refinement are shown in Table 4.

2.3.1. Sample preparation

The processed lithium slag specimens and Corundum was mixed 50% by weight of each along with ethyl alcohol for better particles dispersion, however only raw lithium slag was micronized for 10 minutes because of comparatively bigger particle size and then the particle suspension was heated at 40˚C which is compliant with the method adopted in the literature [6, 24].

Table 4: Parameters for conducting XRD and Rietveld refinement

Instrument		**Bruker D8 Advance (Automated)**
Radiation Source		Cu_Kα (λ=1.504Å, 35kV, 40 mA)
Geniometry range		5-120˚
Step Size		0.013˚
Counting Time		0.7 sec
Rietveld Refinement		**TOPAS (Bruker AXS Version 5)**
Primary and Secondary radius		250 mm
Equatorial Convolution	Angular range	2.944˚
	FDS angle	0.3˚
Axial Convolution	Source length	12 mm
	Primary and secondary Soller	2.3˚

2.4.X-ray Fluorescence

X-ray fluorescence (XRF) is the quantitative elemental analysis technique that gives the quantification of chemical oxide composition. The working principle of both Energy Dispersive X-ray spectroscopy (EDS) and XRF are the same, however, the XRF is quantitative due to usage of a known quantity, chemical composition, and atomic structure of analytical standard crystal [25], however, EDS uses Si-Li detector for identification and semi-quantification of the elements based on stoichiometry. The quantitative natured XRF is usually preferred over semi-quantitative natured EDS due to its higher degree of accuracy and precision for determining elemental composition.

2.4.1. Sample preparation

The quantification of oxide concentration of processed lithium slag was determined by adding 4% of lithium nitrate as an internal standard in it. It is pertinent to mention here that a smooth flat surface is needed for accurate elemental quantification [26]. Therefore, the specimens were converted into glass beads using Spectromelt-MERCK® flux which contains 66 to 34% ratio of Di-lithium tetraborate and Lithium metaborate. The oxide composition was determined at 105˚C. Additionally, the loss

of ignition values of thermo-mechanically processed lithium slag was determined by a robotic Thermo-gravimetric analyzer at a temperature range of 110 to 1000˚C.

2.5.Laser-Diffraction Particle Size Analysis

The particle size distribution of processed lithium slag specimens was achieved by laser-diffraction method using Malvern Panalytical Mastersizer 2000. The state-of-the-art recent technological development in laser diffraction has extended the capability to measure the nano-particle (around 20 nm) [27]. The particle size determination is based on the Mie theory of light scattering [28], which can be interpreted as the smaller particle diffracting light at larger angles than that of bigger particles. A laser beam was bombarded on the ethanol suspended particles and the laser-diffraction pattern of the incident laser beam was collected on a laser diffractometer and particle size is determined by measuring the angular variation of scattered light [27].

2.6.Compressive strength

The mix proportions of lithium slag geopolymer is shown in Table 5. Since the lithium slag geopolymer possesses high gypsum/anhydrite content, its high content causes false setting of geopolymer paste [29, 30]. Therefore, sodium tetraborate decahydrate was added in the mix to retard the setting. The solution of alkaline activators contains 75% sodium silicate and 25% sodium hydroxide by weight. The net water to binder ratio was 0.40.

Geopolymer paste was obtained by mixing processed lithium slag (control, G1, and G1C700) with the liquid alkali activator in a Hobart mixer for 1.5 minutes at 380 rpm. The fresh paste was placed in 50 mm acrylic cubes and compacted in vibrating table. The geopolymer specimens were heat cured at 70˚C for 24 hours and subsequently placed at 25˚C till testing age. The hardened specimens were tested for compressive strength at a loading rate of 0.24 MPa/sec in accordance with ASTM C109 [31].

Table 5: Mix proportions of processed lithium slag geopolymer mixes

Abbreviations	Lithium Slag (kg/m^3)	Sodium Hydroxide (kg/m^3)	Sodium Silicate (kg/m^3)	Ms	Borax (kg/m^3)
Control (Raw-LS)	1212	106	318	3	36

G1-M3	1212	106	318	3	36
G1C700-M3	1212	106	318	3	36

3. Results and Discussion

3.1.Mineralogical composition of lithium slag on processing

The mineral phases constituting lithium slag which were quantified by TIMA and the effect of thermo-mechanical processing on phase transitioning are presented in Table 6 and TIMA micrographs (Figure 3), respectively. It is pertinent to mention that the binding phase of geopolymer is primarily the alumino-silicate species [32, 33] and the available low calcium content of reacting phase in hydrothermal conditions facilitates the formation of semi-zeolitic chained structure [34]. Raw lithium slag is mainly composed of Spodumene, Quartz, Calcite, Anorthite, Muscovite, Albite, and Plagioclase with the mass percentage concentrations of 70.42, 4.66, 4.61, 2.77, 1.22, 1.15, and 0.73 %, respectively. It also contains some fraction of unidentified phase-locked in Spodumene mineral that might be caused by the processing of Spodumene ore for lithium extraction. It primarily contains alumino-silicates in the form Spodumene ($LiAlSi_2O_6$), Anorthite ($CaAl_2Si_2O_8$), Muscovite ($KAl_2(AlSi_3O_{10})(OH)_2$), Albite ($NaAlSi_3O_8$), whereas the traces of alumino-silicates are also locked in Orthoclase ($KAlSi_3O_8$) as well, however, silica exists in the form of Quartz (SiO_2). Moreover, calcium content is mainly associated with the Calcite ($CaCO_3$), and its traces can be found in Anhydrite ($CaSO_4$), Actinolite ($Ca_2Si_8O_{22}(OH)_2$), and Dolomite ($CaMg(CO_3)_2$).

3.1.1. Mineral phase transformation

Grinding of lithium slag imparts chemical reactivity, which is attributed to the reduction in particle size, disorientation of crystals, and creation of some unknown mineral phase due to agglomeration of various minerals constituents [35]. The physical and chemical changes linked with grinding are divided into three phases which are Rittinger's, aggregation, and agglomeration phases [12]. Rittinger's phase is associated with the initial powder grinding in which relatively rapid reduction of particles occurs and the grinding energy is proportional to the surface area of particles.

Upon further grinding, the aggregation phase (reversible change) occurs in which particle' size reduces but the cohesion among particles exists due to the weak Van der Waals forces exists. The ground particles physically aggregate and stick with each other, thus the grinding energy is no more proportional to that of particles' surface area. However, the grinding of powder for a long time induces crystal-transformation (irreversible change) of mineral phases due to strong chemical bonding known as agglomeration.

The SEM micrograph of raw lithium slag presents the presence of larger-sized Spodumene as compared to all other minerals which consequently breakdown physically breakdown into smaller particles as shown in Figure 3. Apart from the physical size reduction upon mechanical grinding, Spodumene chemically converts into other minerals such as Anorthite and unidentified phase because of crystal-transformation of mineral as shown in Table 7. With one hour of grinding of lithium slag, 16.25% of Spodumene is transformed into other minerals. Roughly half of the Spodumene (~8.66%) transformed into unidentified phases, whereas the rest of the Spodumene was converted into Anorthite (~7.62%). Grinding of lithium slag for two hours resulted in further conversion of 11.52% Spodumene to Anorthite. A minute reduction of 0.2% in calcite for grinding the lithium slag between one and two hours, whereas 1.25% reduction was recorded at one-hour grinding.

3.1.2. Effect of reactivity on pre-and post-calcination

Lithium slag shows reactivity due to the amorphousness of alumino-silicate minerals in it. The composition of all the mineral phases is quantified and discussed upon processing, however, it is important to explore the composition of unidentified phase to assess the reactivity of lithium slag. The unidentified phase contains the stoichiometric disproportioning of mineral phases due to thermo-mechanical processing attributed to agglomeration, thus it can be seen as an 'unidentified phase' during EDS spectral matching. A comparison of chemical composition among unidentified phases and other mineral phases is drawn based on their EDS spectra in a ternary plot as presented in Figure 4. Raw lithium slag already contains a smaller

concentration of unidentified phase which is attributed to the processing of Spodumene ore during the lithium extraction process. Most of the unidentified particles possess aluminum to silicon ratios like that of Anorthite, Albite, Muscovite, and Spodumene. However, the unidentified phase also contains the content of calcium in the form of Gypsum, calcite, and Plagioclase marked by the lower silicon content which is identified based on the density of the unidentified phase (2.7g/cc). Raw lithium slag already contains a smaller concentration of unidentified phase which is attributed to the processing of Spodumene ore during the lithium extraction process. The unidentified phase is the most reactive since it forms aggregation, and its maximum concentration can be seen as locked in Spodumene mineral by the phenomenon of aggregation (Figure 3). Not only the unidentified phase, the reactive alumino-silicates present in feldspar (Anorthite, Albite, Plagioclase, Orthoclase) cause it to aggregate within Spodumene mineral. The concentration of the unidentified phase further increases upon thermo-mechanical processing, thus inducing reactivity in lithium slag. Hence, the characterization of the unidentified phase is evident that it majorly contains micro-nano sized alumino-silicate rich particles, some fraction of it is aggregated into other phases due to its reactivity.

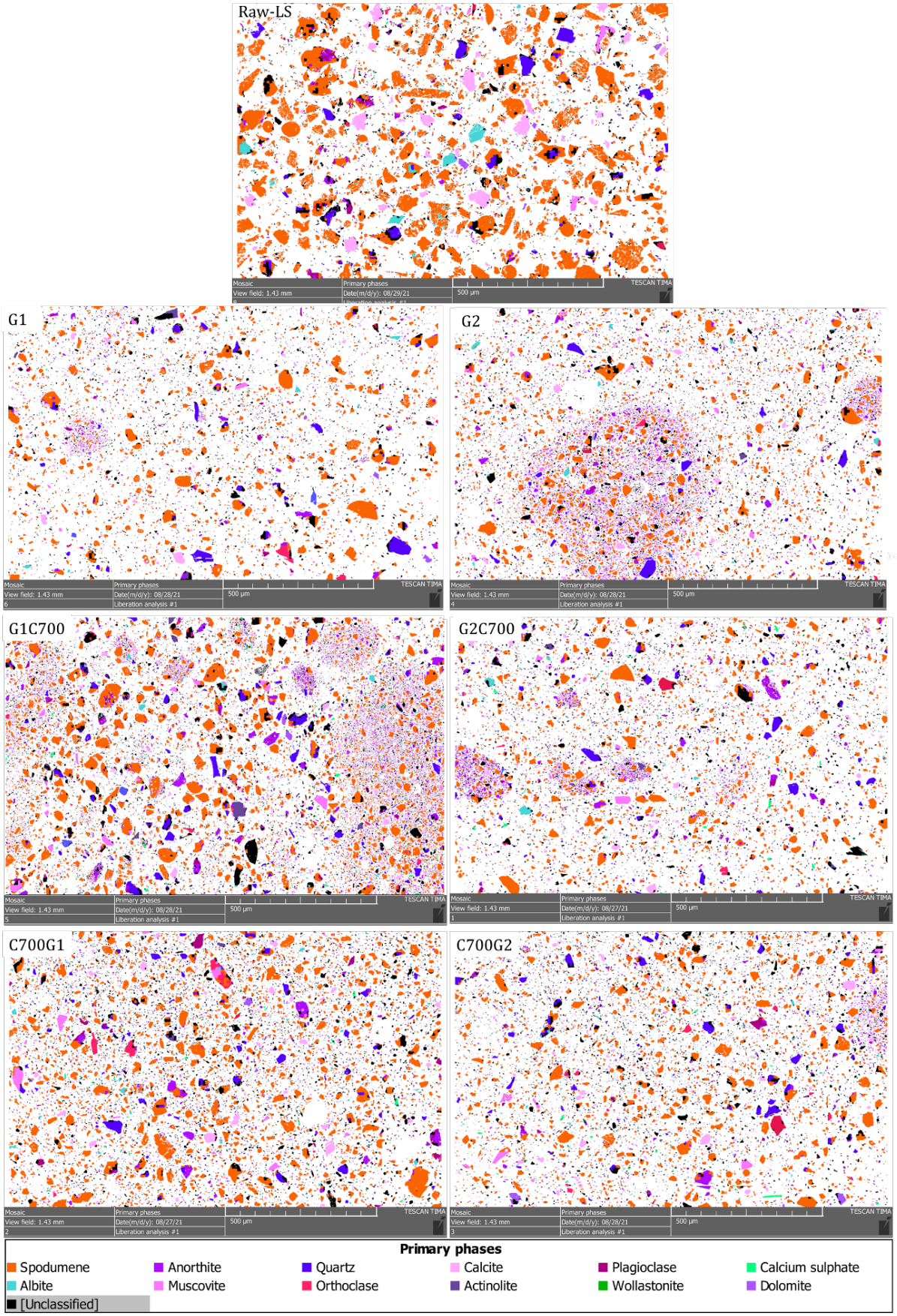

Figure 3: Scanning electron micrographs of raw and thermo-mechanically processed lithium slag

Table 6: Mineral phase composition of lithium slag determined by Tescan Mineral Analyzer (TIMA)

Phases	Raw-LS	G1	G2	G1C700	G2C700	C700G1	C700G2
Spodumene	70.42	54.17	50.25	51.70	52.08	60.08	55.73
Unidentified Phase	12.57	21.23	22.77	21.18	21.44	19.48	21.87
Quartz	4.66	4.97	4.23	5.27	4.43	4.49	4.64
Calcite	4.61	3.36	3.16	2.13	2.85	3.58	3.10
Anorthite	2.77	10.39	14.29	13.23	13.26	6.48	8.92
Muscovite	1.22	1.39	1.23	1.43	1.15	1.02	1.09
Albite	1.15	1.22	1.10	1.19	1.10	1.21	1.18
Plagioclase	0.73	0.99	1.12	1.37	1.43	0.93	1.08
Cumulative of Calcium Sulphate, Orthoclase, Actinolite, Dolomite, Hematite	1.71	2.03	1.56	2.29	2.29	2.17	2.20
Traces	0.16	0.25	0.30	0.22	0.22	0.19	0.18

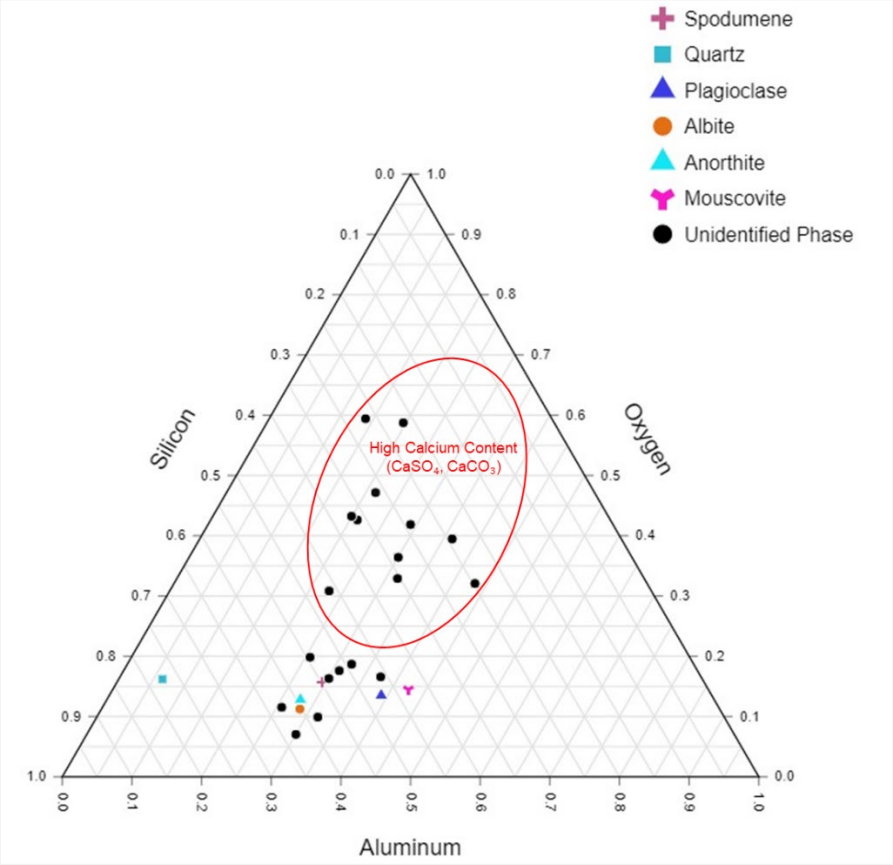

Figure 4: Ternary plot for classification of unidentified phase (density 2.7 g/cc)

Pre-grinding and post-calcination of lithium slag produced a higher transformation of Spodumene to other phases than the lithium slag specimens which were pre-calcined and post-ground. For pre-ground and post-calcined lithium slag, the phase transformation of Spodumene occurred by calcining one-hour ground lithium slag. Spodumene appeared to be reacted with calcite at the thermally elevated condition and 2.84% of it seems to be transformed into Anorthite upon calcination. It is also evident from the literature that the calcination of Spodumene with calcite between 900 and 1100˚C produced Anorthite-like chemical species (Gehlenite) [36], therefore there is some level of transformation of Spodumene and calcite into Anorthite upon thermal treatment. As per literature [14], around 2.5% of the dihydroxylation of phyllosilicate (mica) in lithium slag occurs between 500 and 700˚C, thus increasing the concentration of quartz, Plagioclase, Muscovite, Unidentified phases, and cumulative sum of calcium sulfate, Orthoclase, Actinolite, Dolomite, Hematite by 0.3, 0.38, 0.04, 0.05, and 0.26, respectively. However, the calcination of the 'G2' lithium slag specimen resulted in the increase of 1.83% of Spodumene, Quartz, Muscovite, Plagioclase, and Unidentified phase by 1.83, 0.20, 0.04, and 0.31%, respectively.

It is evident from TIMA micrographs (Figure 3-C700G1, C700G2) that the calcination induced toughness in Spodumene mineral because of occurrence of some degree of vitrification thus reducing the granular disintegration of Spodumene upon its grinding. Moreover, the increase of the Anorthite phase is associated with the disintegration and transformation of Spodumene and calcite, however, the pre-calcination and post-grinding resulted in 60.08, 55.73% of Spodumene for C700G1, C700G2 and was 51.70, 52.08% for G1C700 and G2C700, respectively. While making a comparison between calcination and grinding sequence, it is pertinent to mention that the dominant transformation of Spodumene to other phases was significant in G1C700 (18.72%) compared to that of C700G1 (10.34%) keeping raw lithium slag as a reference. Anorthite mineral phase experienced an abrupt rise in its concentration upon thermo-mechanical processing, which is 10.46% and 3.71% for G1C700 and C700G1 respectively. Similar trends were observed for G2C700 and C700G2 processing

regimes as shown in Table 7. In the case of the unidentified phase, the rise in its concentration for G1C700 and C700G1 comparative to raw lithium slag is 8.61 and 6.91% respectively. TIMA results suggest that the major contribution toward the unidentified phase was attributed to the transformation of Spodumene. If we consider C700G1 as a test case scenario, a total of 10.34% Spodumene phase transformation has occurred in which 6.63% and 3.71% were converted into unidentified and Anorthite phases, respectively. However, the rest of the unidentified phase concentration (0.28%) was attributed to the dihydroxylation of phyllosilicate due to calcination.

Table 7: Phase transformation in lithium slag by thermo-mechanical processing (positive sign indicates gain and negative sign indicates loss)

Phase Transformation	G1	G2	G1C700	G2C700	C700G1	C700G2
Spodumene phase transformation	-16.25	-20.17	-18.72	-18.34	-10.34	-14.69
Total unidentified Phase	+8.66	+10.2	+8.61	+8.87	+6.91	+9.3
Spodumene to unidentified phase	+8.63	+8.65	+8.26	+7.85	+6.63	+8.54
Spodumene to Anorthite	+7.62	+11.52	+10.46	+10.49	+3.71	+6.15

The mineral admixture contains a concentration of silica, alumina, and calcium oxide in variable proportions which has a dominant effect on their reactivity [7]. The aluminum and silicon content present primarily in Spodumene and Anorthite determine the reactivity of lithium slag which is shown in Table 8. Anorthite contains a higher proportion of aluminum than that of Spodumene, whereas the concentration of silicon is the same in both cases. The calcium, silicon, and aluminum contents are associated with feldspar such as Anorthite, Albite, and Plagioclase which have the potential to be geopolymerize into Calcium (Sodium) Alumino Silicate Hydrate (C(N)ASH) gel to impart mechanical strength at low alkaline environment [37]. To better assess the chemical composition of lithium slag and compare with other mineral admixtures, the ternary phase diagram containing silica, alumina, and calcium oxides in lithium slag and data of other precursors (fly ash, Metakaolin, GGBFS) published earlier are shown in Figure 5. In the ternary diagram, the lithium slag exists closer to low calcium geopolymer precursors. However, raw lithium slag contains Si/Al, and Ca/(Si+Al) ratios of 2.59, and 0.11, respectively which are similar to those of fly ash as shown in Table 9. A ratio of Ca/(Si+Al) less than 1 indicates the pozzolanic reactivity

of lithium slag instead of hydration reactivity [11]. Therefore, lithium slag can be classified as a low calcium precursor and its chemical reactivity can be classified as similar to that of fly ash. Conclusively, pre-grinding and post-calcination produce a higher concentration of reactive alumino-silicates in the form of feldspar (primarily Anorthite) than that of pre-calcination and post-grinding regimes. Thus, the former processing regime is suitable for enhancing the reactivity of lithium slag.

Table 8: Elemental Composition of mineral phases

Element	Spodumene	Anorthite	Quartz	Calcite	Albite	Plagioclase
Lithium	3.73	-	-	-	-	-
Oxygen	51.59	38.5	53.26	47.96	48.66	47.27
Aluminum	14.5	18.46	-	-	10.77	9.96
Silicon	30.18	30.2	46.74	-	31.5	31.12
Calcium	-	12.31	-	40.04	0.76	7.4
Carbon	-	-	-	12	-	-
Potassium	-	0.53	-	-		-
Sodium	-	-	-	-	8.3	4.25
Si/Al	2.08	1.64	-	-	2.92	3.12
Density (g/cc)	3.10	2.70	2.60	2.70	2.60	2.70

Table 9: Comparison of raw lithium slag with other mineral admixtures based on oxide composition

Composition	SiO_2	Al_2O_3	CaO	Si/Al	Ca/(Si+Al)
Raw-LS	54.53	21.08	7.53	2.59	0.10
Fly ash	55.3	25.8	2.9	2.14	0.04
Metakaolin	55.01	40.94	0.14	1.34	0.001
GGBFS	32.46	14.3	43.1	2.27	0.92

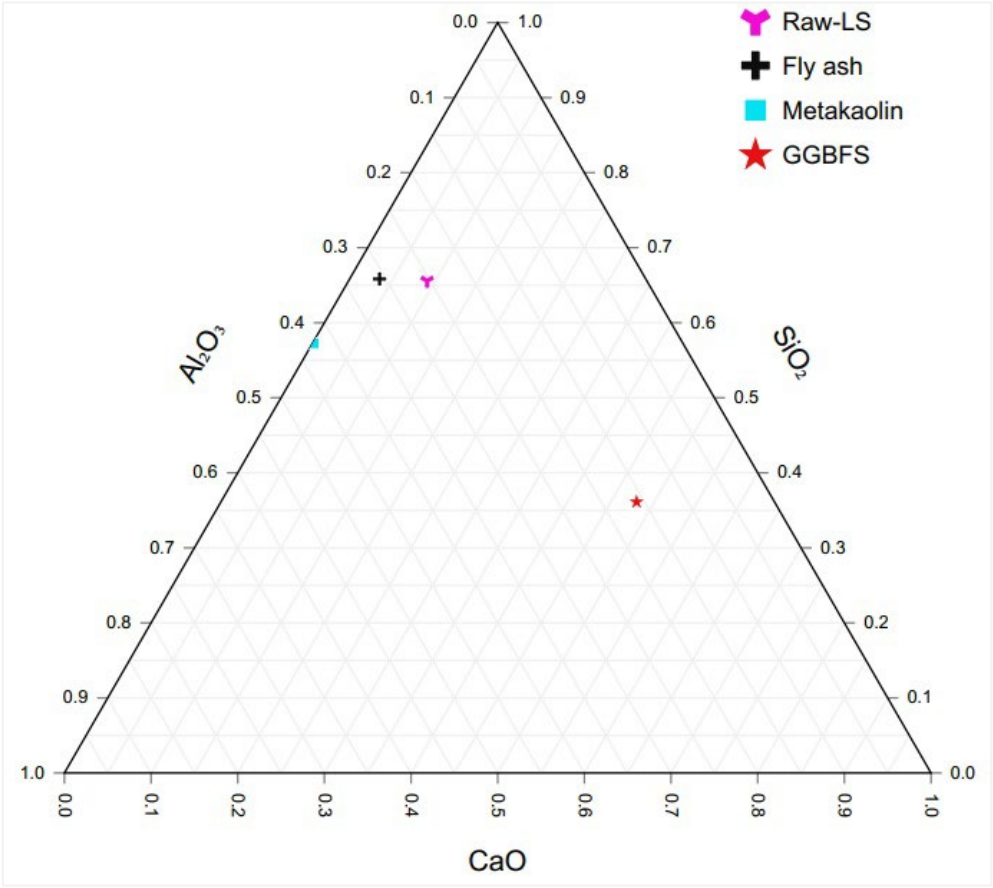

Figure 5: Ternary phase diagram of Ca-SiO_2-Al_2O_3 of processed lithium slag with Metakaolin [38], Fly ash [39], and Ground granulated blast furnace slag (GGBFS) [40] on ternary mapping

3.2.Crystallographic phase identification

The XRD results of processed lithium slag are shown in Figure 6. The main crystallographic phases identified in XRD of lithium slag were Spodumene, Gypsum, Anorthite, and Quartz as shown in Figure 6. Spodumene/β-Spodumene (PDF# 00-039-0049) was identified at Bragg angles (2θ) of 14.73, 19.58, 25.58, 26.63, 28.35, 31.89, 37.77, 43.34, and 48.12˚, Anorthite was detected at 24.04, 26.62, and 77.09˚, Quartz (PDF# 00-046-1045) at 59.90, 80.82˚, and Gypsum (PDF# 04-011-1764) at 29.41, 42.46, 48.35˚. It is pertinent to mention here that corundum was added as an internal standard for crystallographic phase quantification, which is identified at 28.58, 35.14, 37.77, 43.34, 52.53, 57.48, 66.50, 68.20˚ Bragg angles. The crystallographic phases identified in XRD analysis are similar to those determined by literature [6, 41]. Upon thermo-mechanical processing, the peak intensities of Spodumene and Anorthite decreased indicating the increasing amorphousness of alumino-silicate minerals in lithium slag.

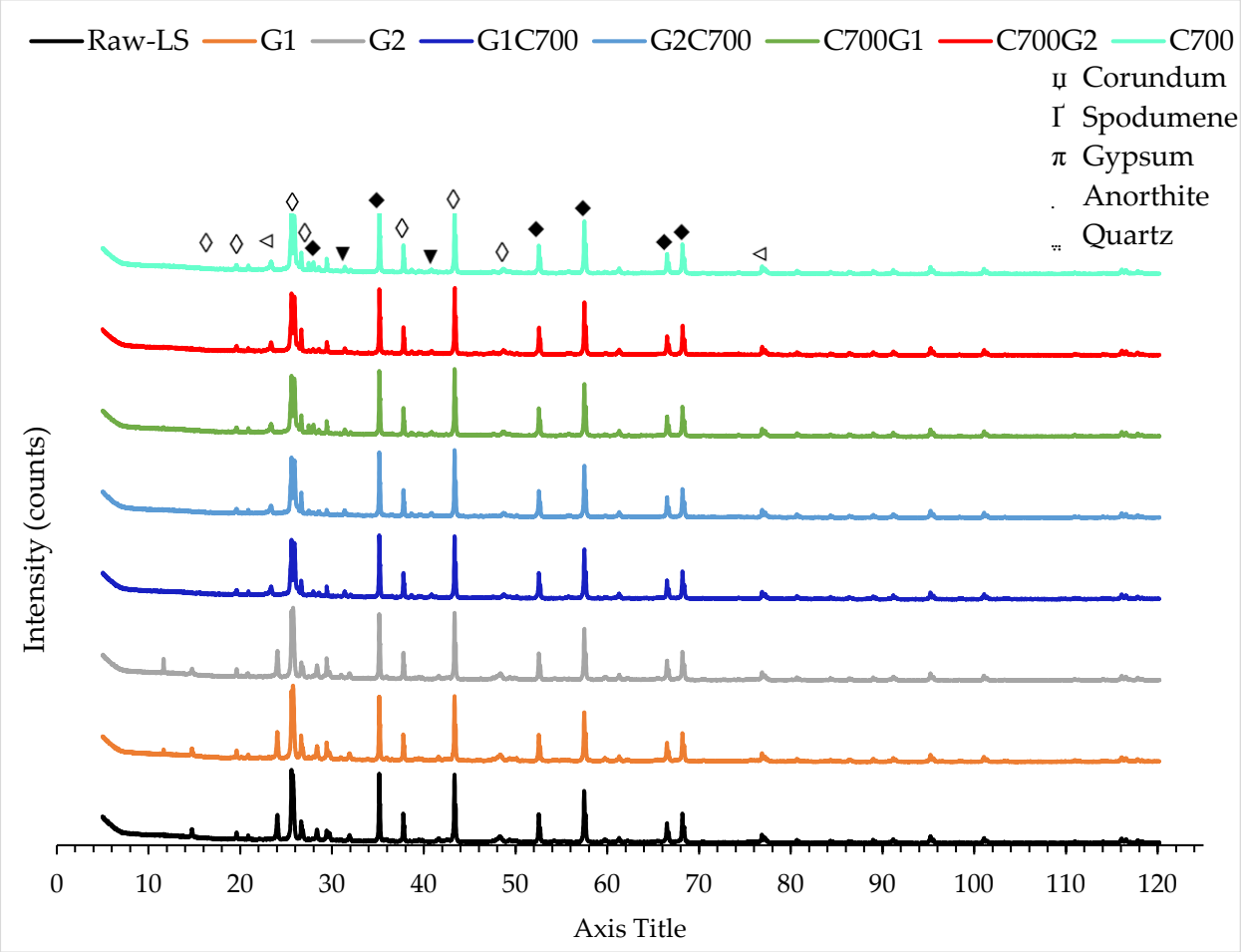

Figure 6: X-ray diffraction of thermo-mechanically processed lithium slag

3.3.Comparison of crystallite sizes

The grinding of lithium slag induces significant changes in the crystal structure such as lattice distortion and chemical composition of minerals [42-45]. The nanosized glassy (amorphous) phase of lithium slag contains zeta potential (surface charge) and the various charged particles stuck together [42]. Upon grinding of lithium slag, the Van der Waals forces become so intense because of the generation of very high local temperature on the crystallites due to mechanical pressure and abrasion during the milling process, thus nanocrystals get crystallized together due to plastic deformations. This chemical phase transformation is known as agglomeration [12]. The agglomeration of the glassy phase in lithium slag can be seen in Figure 7. The concept of agglomeration can be understood by comparing the crystallite size of the various minerals in processed lithium slag determined from Rietveld's refinement. During ball mill grinding, the larger particles were broken down into smaller particles

by initial grinding and the grinding energy is proportionate with the rate of size reduction of particles, upon further grinding the particle size does not reduce with the similar rate due to aggregation followed by agglomeration. This phenomenon of aggregation is also mimicked at particle scale as well as in crystallite sizes of minerals such as Spodumene, Anorthite, and Quartz which are shown in Table 10. It is imperative from the increased crystallite size of Spodumene at one-hour grinding which means that it already passed the limit at which the grinding energy was proportionate with the reduction of particle size, whereas quartz did not undergo the agglomeration at one hour of grinding as the crystallite size reduced and increased at one and two hours of grinding, respectively. Thus, the aggregation of crystals not only depends on the grinding energy but also the abrasion resistance of a particular mineral. Moreover, the calcination of lithium slag before grinding induced resistance to abrasion of Spodumene phase as the crystallite size of Spodumene is higher than that of pre-grinding and post-calcination phase might be due to some level sintering of Spodumene during calcination phase [46]. The agglomeration of crystals is prominent when raw lithium slag was calcined without prior or post-grinding, as a result the Spodumene, Anorthite, Quartz, and Gypsum experience enlargement of crystallite size due to the sintering effect.

3.4.Crystallographic phase quantification

The reactivity of lithium slag also depends upon the formation of glassy (amorphous) phase, concentration, and natural crystallographic phases present in it. Therefore, the Rietveld quantitative analysis of thermo-mechanically processed lithium slag stating the concentration of various crystallographic and amorphous phases are shown in Table 10. Upon thermo-mechanical processing of lithium slag, the considerably high variation of crystal-phase transformation occurred. The concentration of minerals determined in Rietveld refinement and TIMA are different because of the different basic operational principles. The former technique quantifies the mineral phases based on crystallographic properties of minerals, whereas the latter one quantifies the minerals through stoichiometric analysis of the elemental composition achieved from

EDS results. As the intensities of model crystalline structures in the Rietveld refinement are fitted against that of the XRD pattern of the powdered sample by the non-linear least-squares refinement method [19]. It is possible to get closely comparable results of both TIMA and Rietveld refinement only for the purely crystalline powders. However, amorphous materials such as lithium slag possessed crystals defects, deformations, and distortions as a result of thermo-mechanical processing [12]. The model crystal structures couldn't be fitted perfectly with that of observed peaks of uncertain crystal structures of defected minerals in lithium slag, thus, consequently cumulated in the amorphous content. Moreover, the increasing amorphous content upon thermo-mechanical processing was yielded is evidence of crystal defects. It is pertinent to mention various model crystal structures of minerals was tried for Rietveld refinement and presented the results of those which most resembled with the trends of TIMA results.

The plastic deformation in crystallite structure was due to intense temperature at lattice level because of grinding or calcination of lithium slag. Both unidentified phases in TIMA and amorphous phase determined in XRD have comparable trends upon thermo-mechanical processing as shown in Figure 7, thus both phases majorly contain amorphous phase. The difference between amorphous and unidentified phases which was determined from Rietveld refinement and TIMA respectively is significant in combined thermo-mechanical processing which is due to the transformation of crystalline alumino-silicates to amorphous ones.

The concentration of the glassy phase determines the reactivity of lithium slag and the C700 processing regime produced the highest concentration of glassy phase, therefore the highest reactivity is associated with the reactive alumino-silicates present in it. It is worth mentioning that the reactivity of alumina and silica increased at maximum due to calcination around 750°C which is evident from published literature [47]. However, pre-calcination and post-grinding (C700G2) generated a higher concentration of glassy phase than that of pre-grinding and post calcination (G2C700) of lithium slag. Conclusively, the concentration of glassy phase in raw lithium slag

increased upon increasing grinding time. The calcination of grounded lithium slag also produced the glassy phase at both one-and two-hours grinding durations.

Table 10: Rietveld quantitative refinement X-ray diffraction of thermo-mechanically processed lithium slag and comparison of crystallite sizes (Note: Rwp and GoF must be less than 10 and 4, respectively)

Identified Minerals	Spodumene/ Leached-β Spodumene		Anorthite		Quartz		Gypsum		Amorphous Phase	Rwp (Goodness of Fit)
Chemical Formula	$Li.Al(SiO_3)_2$		$CaAl_2Si_2O_8$		SiO_2		$CaSO_4(5H_2O)$			
Parameters	Crystallite size (nm)	Percentage	Crystallite size (nm)	Percentage	Crystallite size (nm)	Percentage	Crystallite size (nm)	Percentage	Percentage	R-values
Raw-LS	26.38	33.18	27.58	17.16	28.01	18.32	17.23	3.32	28.04	8.30 (2.12)
G1	89.79	2.4	67.34	25.66	17.81	33.1	14.05	5.18	33.66	8.62 (2.21)
G2	227.6	2.84	57.34	22.28	44.89	30.9	36.47	5.76	38.22	8.67 (2.23)
G1C700	67.34	2.58	67.34	14.66	89.79	28.9	75.17	1.4	52.46	5.90 (1.51)
G2C700	118.46	1.92	66.34	11.52	8.35	23.62	31.05	0.74	62.2	5.97 (1.55)
C700G1	118.46	2.54	67.34	17.76	44.89	24.44	87.29	3.52	51.76	5.38 (1.39)
C700G2	76.08	0.92	22.48	10.28	8.81	10.18	99.72	3.26	75.36	5.45 (1.48)
C700	89.67	2.01	67.34	8.35	40.8	6.59	52.51	1.46	81.57	6.15 (1.98)

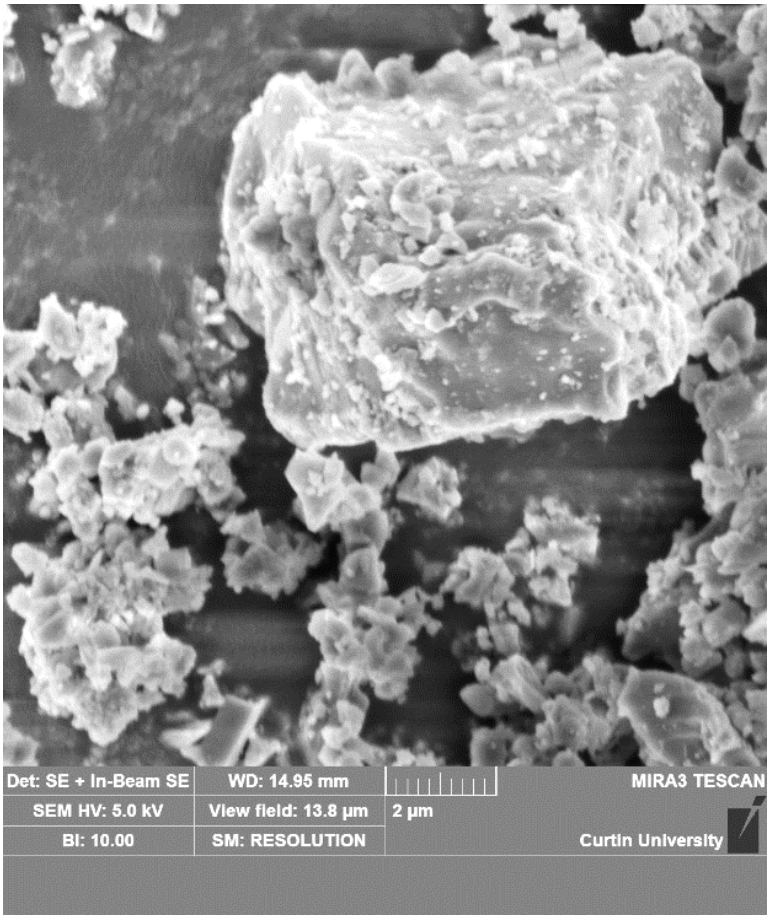

Figure 7: Amorphous phase generation by agglomeration and particle crystallization due to thermo-mechanical processing of lithium slag

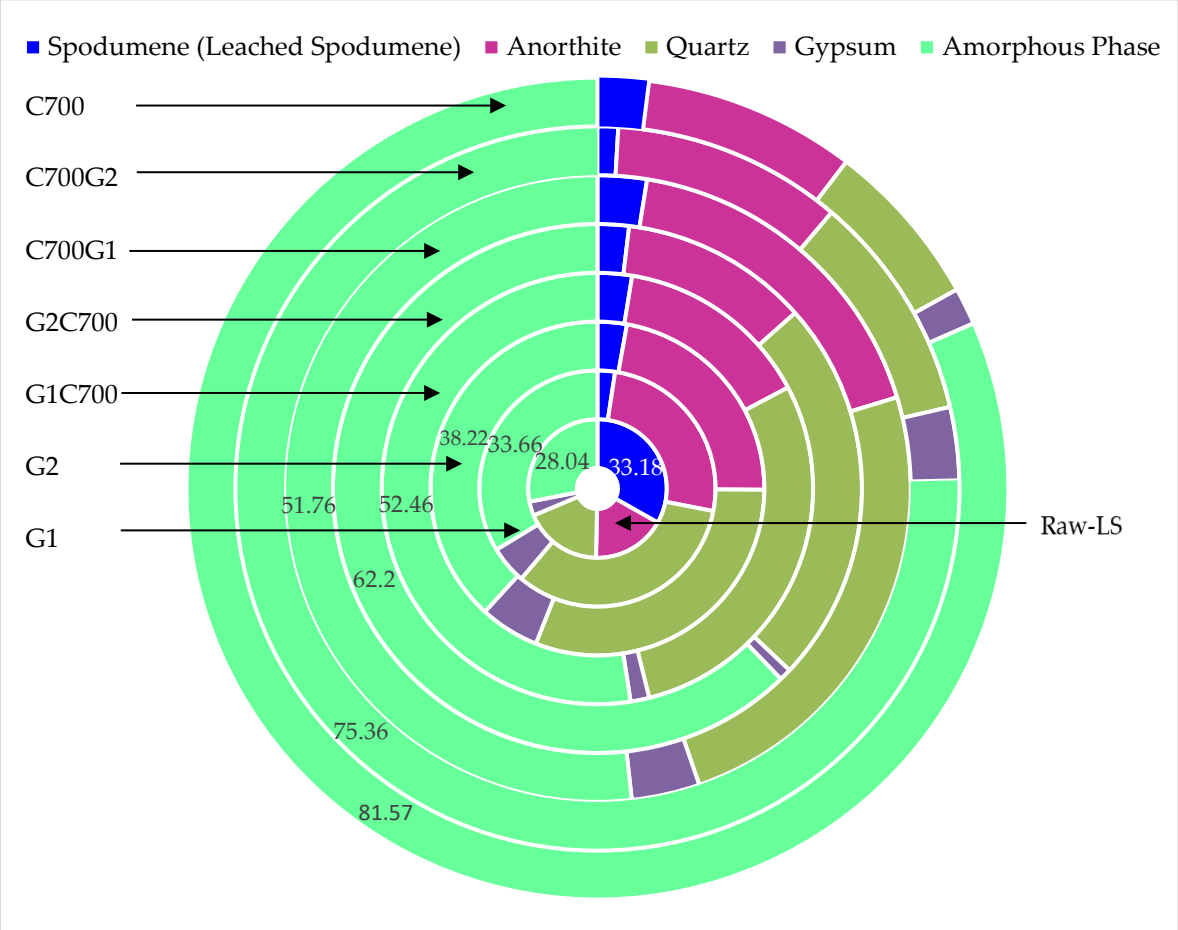

Figure 8: Percentage mass quantification of crystallographic phases of thermo-mechanically processed lithium slag by Rietveld refinement

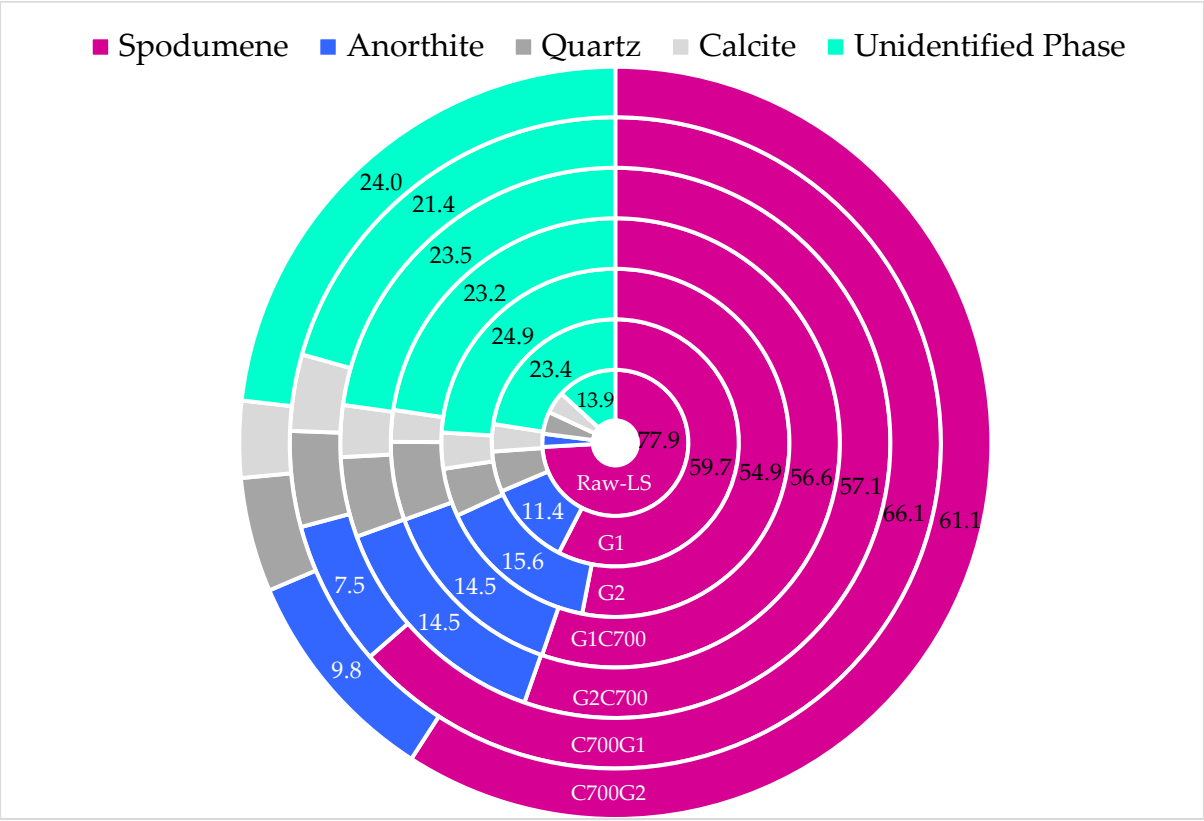

Figure 9: Percentage mass of mineral phase composition by TIMA

3.5.Chemical composition and particle size distribution

The oxide composition of processed samples which was determined from TIMA and XRF is shown in Table 11. Because of the quantitative nature of the XRF technique, the oxide composition determined in TIMA-EDS analysis is compared with that of XRF analysis. The results indicated that the chemical oxide composition determined from both techniques produced considerable statistically accurate results. The results determined from both XRF and TIMA-EDS for processed lithium slag with the maximum absolute difference value of approximately 5% were recorded which endorse the accuracy of automated Scanning Electron Microscopy. Higher values of absolute difference were raised only for oxides of sulfur and calcium. As the calcium and sulfate content is associated with gypsum/anhydrite as evident in XRD and Rietveld quantitative analysis, however the particle shape of gypsum/anhydrite is prismatic as evident in SEM analysis conducted by Liu et al. [17]. Apart from the state-of-the-art capabilities of TIMA, one of its inherent limitations is that it couldn't provide the accurate chemical composition of needle-like or prismatic particles in a mix of heterogeneous shape particles unlike that of a bulk powder analysis such as XRF. TIMA determined the chemical composition based on quantitative EDS results from a cross-section of polished and carbon-coated epoxy impregnated resin-block containing powdered lithium slag (section 2.2.1). It is practically not possible for the prismatic particles (anhydrite/gypsum) to be aligned along the cross-section of the resin block in a way to have maximum exposure to EDS's X-rays. The quantitative results of XRF revealed that the cumulative concentration of silica, alumina, and iron oxides in raw lithium slag is above 77.06% which qualifies the chemical concentration for a pozzolan as per ASTM C618 [8]. However, the cumulative concentration of silica, alumina and iron oxides increased from 77.40 to 80.33% upon calcination, this might be due to the dihydroxylation of phyllosilicate (mica) between 500-700˚C. Moreover, the effect of pre and post calcination has negligible effects on the cumulative oxide concentration of silica, alumina, and iron.

The results of laser-diffracted particle distribution analysis and TIMA particle size distribution of processed lithium slag are shown in Table 12. Based on the resolution of imaging in TIMA (pixel size 1μm), results depict that the D_{50} value determined in TIMA generally remained higher than that of laser-diffracted particle size analysis, thus the nano-sized lithium slag particles didn't participate in cumulative particle size distribution which can be seen in Figure 10 (e-h). The particle size of over 1 μm was determined in TIMA as the pixel size (1 μm) is the determinant factor for both analysis time and least particle measuring capability. However, the selection of pixel size did not impact much on D_{50} values as the maximum difference remained around 5μm as shown in Table 12. The frequency size distribution curves of lithium slag in the case of laser diffraction method depict that the particle aggregation significantly affected the accurate determination of particle frequencies, whereas frequency size distribution curves in TIMA (Figure 10, e-h) were least influenced marked by higher particle frequencies.

The one-hour grinding of raw lithium slag produced a significant reduction of particle size in which D_{50} value dropped from 43.15 to 8.90 μm as per the result of laser particle size distribution analysis. However, upon further grinding (2-hr) the reduction of size was not significant to that of the former case because raw lithium slag advanced through Rittinger and aggregation phases in one hour of grinding contrary to that of two-hour grinding in which the agglomeration phase transformation occurred, where the grinding energy was no more proportionate with that of the surface area of lithium slag as explained earlier in section 3.1.1. It is pertinent to mention here that the particles get fused into each other via chemical bonding during agglomeration phase transformation, thus the further grinding of lithium slag might be considered as inefficient processing.

Calcination of 1-hour ground lithium slag increases the D_{50} value from 8.91 to 13.21 μm due to agglomeration at particle as well as atomic-level as evident from Rietveld refinement. Similar trends of agglomeration were observed in the case of two hours of calcination. Pre-calcination post grinding produced a higher particle size than that

of an inverse case due to the sintering of particles [46]. Moreover, the particle agglomeration is compliant with that of trends of atomic crystallite sizes which endorses the crystal transformation in lithium slag during processing. Hence, the two-hour grinding does not reduce the particle size of lithium slag significantly attributed to agglomeration occurring at crystallite level, thus one-hour grinding can be adopted for improving the reactivity of lithium slag by milling process.

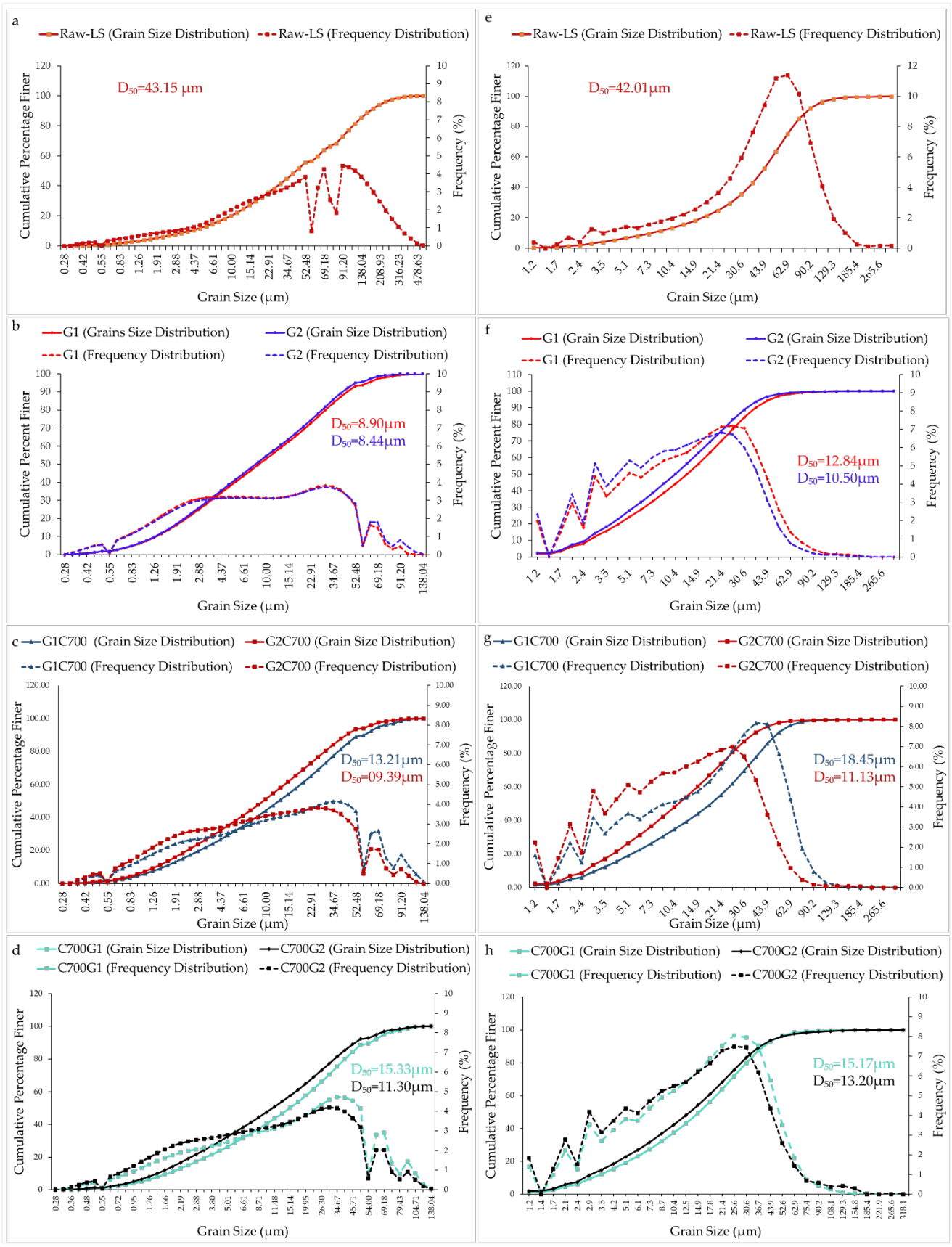

Figure 10: Frequency and particle size distribution of processed lithium slag determined from laser-particle size distribution (a to d) and TIMA (e to h)

Table 11: Oxide composition determined from EDS and XRF ([a] Absolute difference more than 6%)

Oxide		SiO2	Al2O3	Fe2O3	CaO	MgO	TiO2	SO3	K2O
TIMA	Raw-LS	57.42	17.43	0.33	12.92	0.56	0.05	0.11	0.61
XRF		54.53	21.08	1.45	7.535	0.575	0.05	5.62	0.88
Difference		2.89	3.65	1.12	5.38 [a]	0.02	0.00	5.51 [a]	0.28
TIMA	G1	55.61	21.07	0.50	13.66	0.39	0.04	0.02	0.75
XRF		54.81	21.24	1.35	7.85	0.62	0.06	5.45	0.89
Difference		0.80	0.17	0.85	5.81[a]	0.23	0.02	5.43 [a]	0.14
TIMA	G2	56.68	19.63	0.87	13.64	0.54	0.03	0.03	0.75
XRF		54.65	21.06	1.37	7.72	0.60	0.06	5.40	0.89
Difference		2.03	1.43	0.50	5.92 [a]	0.06	0.03	5.37 [a]	0.14
TIMA	G1C700	57.39	20.61	0.92	12.03	0.44	0.03	0.31	0.67
XRF		56.87	22.05	1.41	8.19	0.65	0.07	5.64	0.93
Difference		0.52	1.44	0.49	3.84	0.21	0.04	5.33 [a]	0.26
TIMA	G2C700	55.88	20.69	0.84	13.67	0.36	0.03	0.41	0.62
XRF		56.96	22.10	1.58	8.27	0.66	0.07	5.75	0.93
Difference		1.08	1.41	0.74	5.40	0.30	0.04	5.34 [a]	0.31
TIMA	C700G1	56.92	18.87	0.67	12.42	0.40	0.03	0.52	0.56
XRF		56.76	21.94	1.42	8.11	0.64	0.06	5.64	0.92
Difference		0.16	3.07	0.75	4.31	0.24	0.03	5.12 [a]	0.36
TIMA	C700G2	56.89	19.43	0.64	12.76	0.43	0.03	0.50	0.60
XRF		56.62	21.86	1.45	8.11	0.64	0.06	5.67	0.92
Difference		0.27	2.43	0.81	4.65	0.21	0.03	5.17 [a]	0.32

Table 12: Comparison of D_{50} values determined by TIMA and PSDA

Processed Slag	TIMA D_{50}	PSDA D_{50}	Difference (μm)
Raw	42.01	43.15	1.14
G1	12.84	8.90	3.93
G2	10.5	8.44	2.05
G1C700	18.45	13.21	5.24
G2C700	11.13	9.39	1.74
C700G1	15.17	15.33	0.16
C700G2	13.2	11.32	1.88

3.6. Compressive Strength

Compressive strengths of the lithium slag geopolymer pastes are shown in Figure 11. The compressive strength of control, G1, and G1C700 lithium slag geopolymers were 1.22, 9.34, and 11.80 MPa, respectively. The compressive strength of raw lithium slag geopolymer was recroded minimum as 1.22 MPa, however the compressive strengths

of G1-M3 and G1C700-M3 geopolymer pastes were 9.34 and 11.80 MPa, respectively. The processing of lithium slag resulted in significantly higher compressive strength because of the intrinsic change in physical properties and chemical composition of lithium slag upon combined and separate effect of thermal and mechanical processing. The grinding of lithium slag for one hour increased the reactivity which is attributed to reduction in the particle size from 43.15 μm to 8.90 μm. It is pertinent to mention that the calcination of lithium slag resulted in the generation of amorphous phase over 51% which primarily contains aluminosilicates that enhanced its reactivity. Although the prominent compressive strength enhancement was resulted upon thermo-mechanical processing, however the compressive strength generally remained lower comparative to fly ash based geopolymer [48, 49], which is attributed to high sulphate content in lithium slag. The higher sulphate content in the form of anhydrite/gypsum caused the false setting of geopolymer paste, thus the higher porosity. This factor is being investigated in addition to use additional source materials e.g. fly ash, silica fume, etc. with processed lithium slag and will be published in future research.

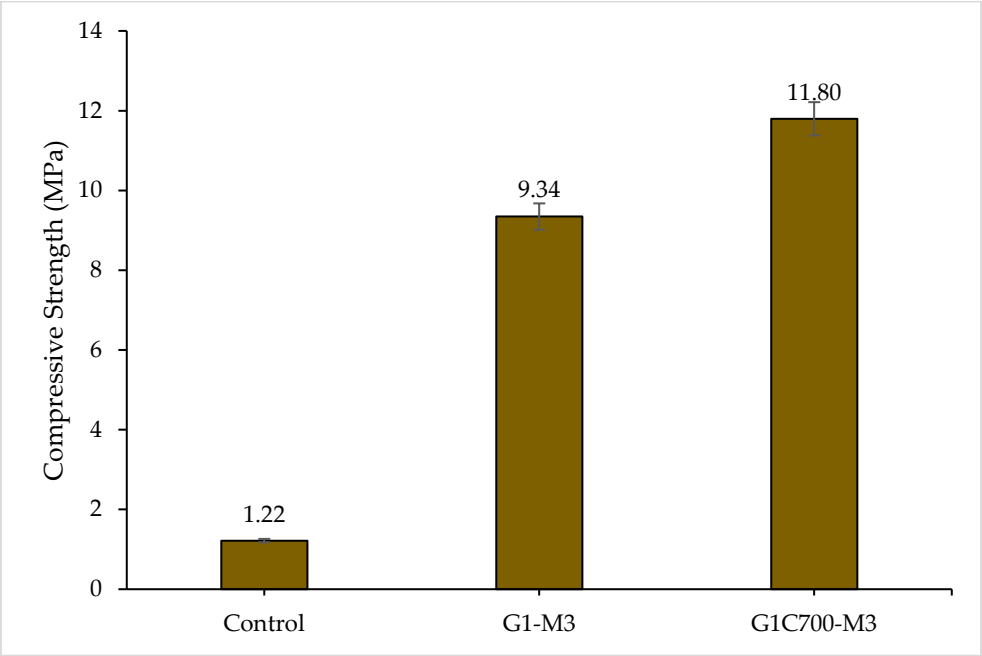

Figure 11: Compressive strength of processed lithium slag geopolymer pastes

3.7.Energy intensity and carbon emissions

The energy intensity and carbon emission associated with the thermo-mechanical processing of lithium slag is calculated in the case of Western Australia, where 656.4 grams of carbon emissions are enhanced in the atmosphere upon production of one kW.h of electricity [50]. Moreover, the calcination of lithium slag took 5.39 hours while adopting a ramp temperature rate of 3°C/min and a hold time of 2 hours at 700°C. It is worth mentioning that the kiln is used to consume half of the power during the ramp mode of operation. That's why even at a higher calcination time than grinding, the energy intensity and carbon emissions are lower than that of grinding. However, the energy intensities and carbon emission during one-hour grinding and calcination are comparable which can be seen in Table 12. The one-hour grinding and calcination consumed 0.67 and 0.62 kW.h of power per kilogram processing of lithium slag, thus contributing 0.44 and 0.41 kilograms of CO_2, respectively. Hence, two hours of grinding of lithium can be considered as an energy-intensive processing regime, therefore one-hour grinding can be preferred over the former one.

The formation of amorphous aluminosilicates (glassy phase) in lithium slag induces chemical reactivity, therefore it becomes more suitable for geopolymer precursor. The concentration of the amorphous phase is proportionate with the thermo-mechanical processing but its over-processing in terms of carbon emissions can mark it as an energy-intensive precursor. Considering carbon emissions of thermo-mechanical processing, the phase transformation of Spodumene to Anorthite (+10.46%) and amorphous phase (+8.26%) is dominant in G1C700 after G2 like that of trends of Rietveld refinement, moreover, the average particle size of G1C700 is 13.21 micron which is comparable to least detected D_{50} value (8.44 micron). Thus, G1C700 can be classified as an energy-efficient processed regime in perspective of carbon emissions and chemical reactivity.

Table 13: Carbon emissions associated with the processing of lithium slag

	Machine Power (kW)	Time (hrs)	Power (kW.h)	Energy Intensity (kW.h/kg)	Carbon Emissions ($kgCO_2$/kg of LS)
	1.00	1.00	1.00	0.67	0.44

Ball Mill		2.00	2.00	1.33	0.88
Furnace	1.02	5.39	3.75	0.62	0.41

4. Conclusion

Thermo-mechanical processing of lithium slag induces reactivity by reduction of average grain size and mineral phase transformation. However, the detailed conclusions are as follows:

1. Quantification of mineral and crystallographic phases by TIMA and Rietveld quantitative refinement, respectively, and correlating both techniques can synergically be used for assessing the reactivity of various other mineral admixtures.
2. The stoichiometric calculation of elemental and mineral composition determined by TIMA is correlated with that of the XRF technique (quantitative). The results suggest the considerable statistical significance of the TIMA technique as the absolute difference between oxide content remained around 5% alongside TIMA's state-of-the-art interactive microanalysis and automated SEM/EDS measurements.
3. As the concentration of the amorphous phase determines the reactivity of mineral admixture, TIMA is a state-of-the-art technique for characterizing unidentified phases and helps to associate mineral composition with other morphological features such as particle shape and size. Thus, it is also used in material characterization and processing techniques alongside its use in various other application areas.
4. The major mineralogical and crystallographic phases detected in lithium slag were Spodumene/β-Spodumene, Anorthite, Quartz, Calcite, Muscovite, and Albite. The trends of concentration of amorphous and unidentified phases determined by TIMA and XRD, respectively are comparable in each of the processed lithium slag regimes. The concentration of the amorphous phase is proportionate with the thermo-mechanical processing energy. The difference between amorphous and unidentified phases is significant in combined thermo-mechanical processing which is due to the transformation of crystalline

alumino-silicates to amorphous ones. Therefore, both mentioned phases majorly contain glassy/amorphous aluminosilicates.

5. The preliminary results show that compressive strength of lithium slag geopolymer improved significantly by thermal and mechanical processing of the slag. This is attributed to the reduction in particle size and chemical phase transformation of lithium slag. The reactivity of lithium slag in geopolymer by calorimetric tests and its detailed investigation on the development of mechanical properties will be performed in the future.
6. Crystallographic and mineralogical phase transformation occurred by grinding and calcination attributed to chemical phase transformation known as agglomeration. Considering carbon footprints of thermo-mechanical processing the phase transformation of Spodumene to Anorthite (+10.46%) and amorphous phase (+8.26%) is dominant in G1C700, similar to that of results of Rietveld refinement, thus G1C700 can be classified as an energy-efficient processed regime along with 0.45 kg of carbon emissions per kilogram of processed lithium slag.
7. The accurate particle distribution can be achieved through TIMA by selecting pixel size closer to the least powder's particle size fraction, however smaller pixel size might drastically increase the analysis time. The average particle size of G1C700 is 13.21 micron which is comparable to the least D_{50} value (8.44 micron). The grinding energy is certainly not proportionate in a two-hour grinding regime due to the agglomeration of crystallites, thus increasing the particle size. Therefore, minimal crystallite agglomeration might have occurred in one hour grinding too, however more research is suggested for less than one hour grinding of lithium slag to reduce crystal agglomeration and hence the optimum grinding.

Acknowledgment

The authors acknowledge to Australian Research Council (ARC) for providing financial support in this research in the form of Discovery Project grant DP200102784. Most part this research was undertaken using TESCAN Integrated Mineral Analyzer (TIMA, ARC LE140100150) and X-ray diffractometer at John De Laeter Centre at Curtin University Australia.

CRedit author contribution statement

Usman Javed: Conceptualization, Data curation, Formal analysis, Investigation, Methodology, Visualization, Writing-original draft. **Faiz Uddin Ahmed Shaikh**: Conceptualization, Funding acquisition, Project administration, Resources, Validation, Supervision, Writing-review & editing. **Prabir Sarker:** Supervision, Validation, Resources, Writing-review & editing.

References:

[1] K.E. Aifantis, S.A. Hackney, R.V. Kumar, High energy density lithium batteries, Wiley Online Library2010.
[2] D.E. Garrett, Handbook of lithium and natural calcium chloride, Elsevier2004.
[3] D. Champion, Australian Resource Reviews: Lithium Geoscience Australia, in: G. Australia (Ed.)Canberra, 2018.
[4] B.W. Jaskula, 2017 Minerals Yearbook, in: U.S.D.o.t.I. (USGS) (Ed.), 2020.
[5] I.a.S. Department of Industry, Resources and Energy Quarterly 2019a.
[6] Z. Liu, J. Wang, Q. Jiang, G. Cheng, L. Li, Y. Kang, D. Wang, A green route to sustainable alkali-activated materials by heat and chemical activation of lithium slag, Journal of Cleaner Production, 225 (2019) 1184-1193.
[7] W. Yiren, W. Dongmin, C. Yong, Z. Dapeng, L. Ze, Micro-morphology and phase composition of lithium slag from lithium carbonate production by sulphuric acid process, Construction and Building Materials, 203 (2019) 304-313.
[8] A. C618, International. Standard specification for coal fly ash and raw or calcined natural pozzolan for use in concrete, American Society for Testing and Materials West Conshohocken, 2012.
[9] K. Alexander, J. Wardlaw, I. Ivanusec, The influence of SO3 content of Portland cement on the creep and other physical properties of concrete, Cement and Concrete Research, 9 (1979) 451-459.
[10] H.F. Taylor, Cement chemistry, Thomas Telford London1997.
[11] S. Nath, S. Kumar, Evaluation of the suitability of ground granulated silico-manganese slag in Portland slag cement, Construction and Building Materials, 125 (2016) 127-134.
[12] L. Opoczky, Fine grinding and agglomeration of silicates, Powder Technology, 17 (1977) 1-7.
[13] S. Knickerbocker, M.R. Tuzzolo, S. Lawhorne, Sinterable β-Spodumene Glass-Ceramics, Journal of the American Ceramic Society, 72 (1989) 1873-1879.
[14] Z. Liu, J.-x. Wang, L. Li, D.-m. Wang, Characteristics of Alkali-Activated Lithium Slag at Early Reaction Age, Journal of Materials in Civil Engineering, 31 (2019) 04019312.
[15] A. C-618, American Society for Testing and Materials, ASTM Specification for Fly Ash and Raw or Calcined Natural Pozzolan for use as a Mineral Admixture in Portland Cement Concrete, Designation C618, ASTM international Philadelphia, 2002.
[16] L. Keyte, Fly ash glass chemistry and inorganic polymer cements, Geopolymers, Elsevier2009, pp. 15-36.
[17] Z. Liu, Wang, Jixiang, Jiang, Qikan, Cheng, Guodong, Li, Li, Kang, Yixing, Wang, Dongmin, A green route to sustainable alkali-activated materials by heat and chemical activation of lithium slag, Journal of Cleaner Production, 225 (2019) 1184-1193.
[18] J.L. Provis, J.S.J. Van Deventer, Geopolymers: structures, processing, properties and industrial applications, Elsevier2009.
[19] M.G. Aylmore, Automated mineralogy, SME Mineral Processing & Extractive Metallurgy Handbook; Dunne, RC, Kawatra, SK, Young, CA, Eds, (2019) 43-68.
[20] B. Schulz, D. Sandmann, S. Gilbricht, SEM-based automated mineralogy and its application in geo-and material sciences, Minerals, 10 (2020) 1004.
[21] M.G. Aylmore, K. Merigot, W.D. Rickard, N.J. Evans, B.J. McDonald, E. Catovic, P. Spitalny, Assessment of a spodumene ore by advanced analytical and mass spectrometry techniques to determine its amenability to processing for the extraction of lithium, Minerals Engineering, 119 (2018) 137-148.

[22] L. Tchadjie, S. Ekolu, Enhancing the reactivity of aluminosilicate materials toward geopolymer synthesis, Journal of materials science, 53 (2018) 4709-4733.
[23] K. Kjellsen, A. Monsøy, K. Isachsen, R. Detwiler, Preparation of flat-polished specimens for SEM-backscattered electron imaging and X-ray microanalysis—importance of epoxy impregnation, Cement and concrete research, 33 (2003) 611-616.
[24] A. Fernández-Jimenez, A. De La Torre, A. Palomo, G. López-Olmo, M. Alonso, M. Aranda, Quantitative determination of phases in the alkali activation of fly ash. Part I. Potential ash reactivity, Fuel, 85 (2006) 625-634.
[25] S. Nasrazadani, S. Hassani, Modern analytical techniques in failure analysis of aerospace, chemical, and oil and gas industries, Handbook of Materials Failure Analysis with Case Studies from the Oil and Gas Industry, (2016) 39-54.
[26] U. Kramar, X-Ray fluorescence spectrometers, (2017).
[27] Malvern, Mastersizer 2000 data sheet, Malvern Instruments, 2007.
[28] G. Mie, Annalen der Physik. 1908, B, 25 377-445.
[29] J. Wang, L. Han, Z. Liu, D. Wang, Setting controlling of lithium slag-based geopolymer by activator and sodium tetraborate as a retarder and its effects on mortar properties, Cement and Concrete Composites, 110 (2020) 103598.
[30] F.U.S. Usman Javed, Prabir Sarker, Microstructural investigation of lithium slag geopolymer pastes containing silica fume and fly ash as an additive chemical modifiers Cement and Concrete Composites, (2022).
[31] A. C109/C109M, Standard Test Method for Compressive Strength of Hydraulic Cement Mortars (Using 2-in. or [50 mm] Cube Specimens)1, 2022.
[32] P. Duxson, J.L. Provis, G.C. Lukey, F. Separovic, J.S. van Deventer, 29Si NMR study of structural ordering in aluminosilicate geopolymer gels, Langmuir, 21 (2005) 3028-3036.
[33] H. Rahier, W. Simons, B. Van Mele, M. Biesemans, Low-temperature synthesized aluminosilicate glasses: Part III Influence of the composition of the silicate solution on production, structure and properties, Journal of Materials Science, 32 (1997) 2237-2247.
[34] J.L. Provis, G.C. Lukey, J.S. van Deventer, Do geopolymers actually contain nanocrystalline zeolites? A reexamination of existing results, Chemistry of materials, 17 (2005) 3075-3085.
[35] V. Boldyrev, K. Tkáčová, Mechanochemistry of solids: past, present, and prospects, Journal of materials synthesis and processing, 8 (2000) 121-132.
[36] G. White, T. McVay, Some aspects of the recovery of lithium from spodumene, Oak Ridge National Lab., Tenn., 1958.
[37] D. González-García, L. Téllez-Jurado, F. Jiménez-Álvarez, H. Balmori-Ramírez, Structural study of geopolymers obtained from alkali-activated natural pozzolan feldspars, Ceramics International, 43 (2017) 2606-2613.
[38] P. He, M. Wang, S. Fu, D. Jia, S. Yan, J. Yuan, J. Xu, P. Wang, Y. Zhou, Effects of Si/Al ratio on the structure and properties of metakaolin based geopolymer, Ceramics international, 42 (2016) 14416-14422.
[39] G.S. Ryu, Y.B. Lee, K.T. Koh, Y.S. Chung, The mechanical properties of fly ash-based geopolymer concrete with alkaline activators, Construction and building materials, 47 (2013) 409-418.
[40] P. Nath, P.K. Sarker, Effect of GGBFS on setting, workability and early strength properties of fly ash geopolymer concrete cured in ambient condition, Construction and Building materials, 66 (2014) 163-171.
[41] B. Li, R. Cao, N. You, C. Chen, Y. Zhang, Products and properties of steam cured cement mortar containing lithium slag under partial immersion in sulfate solution, Construction and Building Materials, 220 (2019) 596-606.

[42] J. Meng, L. Xu, L. Luo, K. Shu, Effects of grinding media on the flotation behavior of spodumene in mixed anionic/cationic collectors system, Colloids and Surfaces A: Physicochemical and Engineering Aspects, 627 (2021) 127213.
[43] G. Zhu, Y. Wang, X. Liu, F. Yu, D. Lu, The cleavage and surface properties of wet and dry ground spodumene and their flotation behavior, Applied Surface Science, 357 (2015) 333-339.
[44] G.-l. Zhu, Y.-h. Wang, X.-m. Wang, J.D. Miller, D.-f. Lu, X.-y. Zheng, Y.-h. Zhao, H.-t. Zheng, Effects of grinding environment and lattice impurities on spodumene flotation, Transactions of Nonferrous Metals Society of China, 29 (2019) 1527-1537.
[45] M. Peltoniemi, R. Kallio, A. Tanhua, S. Luukkanen, P. Perämäki, Mineralogical and surface chemical characterization of flotation feed and products after wet and dry grinding, Minerals Engineering, 156 (2020) 106500.
[46] T. Ogiwara, Y. Noda, O. Kimura, Low-Temperature Sintering of β-Spodumene Ceramics Using Li 2 O–GeO 2 as a Sintering Additive, Journal of the American Ceramic Society, 96 (2013) 2577-2582.
[47] P. Perumal, K. Piekkari, H. Sreenivasan, P. Kinnunen, M. Illikainen, One-part geopolymers from mining residues–Effect of thermal treatment on three different tailings, Minerals Engineering, 144 (2019) 106026.
[48] L.N. Assi, E.E. Deaver, M.K. ElBatanouny, P. Ziehl, Investigation of early compressive strength of fly ash-based geopolymer concrete, Construction and Building Materials, 112 (2016) 807-815.
[49] M.N. Hadi, M. Al-Azzawi, T. Yu, Effects of fly ash characteristics and alkaline activator components on compressive strength of fly ash-based geopolymer mortar, Construction and Building Materials, 175 (2018) 41-54.
[50] I. Tiseo, Power sector carbon intensity outlook in Australia 2020-2050, 2021.